Article

Highly Sensitive and Selective Detection of Hydrogen Using Pd-Coated SnO$_2$ Nanorod Arrays for Breath-Analyzer Applications

Hwaebong Jung [1], Junho Hwang [1], Yong-Sahm Choe [2], Hyun-Sook Lee [1],* and Wooyoung Lee [1],*

[1] Department of Materials Science and Engineering, Yonsei University, 50 Yonseiro, Seodaemun-gu, Seoul 03722, Korea; interfd@yonsei.ac.kr (H.J.); turtlesoup@yonsei.ac.kr (J.H.)
[2] Isenlab Inc., Halla Sigma Valley, Dunchon-daero 545, Jungwon-gu, Seongnam-si 13215, Korea; cys@isenlab.com
* Correspondence: h-slee@yonsei.ac.kr (H.-S.L.); wooyoung@yonsei.ac.kr (W.L.)

Abstract: We report a breath hydrogen analyzer based on Pd-coated SnO$_2$ nanorods (Pd-SnO$_2$ NRs) sensor integrated into a miniaturized gas chromatography (GC) column. The device can measure a wide range of hydrogen (1–100 ppm), within 100 s, using a small volume of human breath (1 mL) without pre-concentration. Especially, the mini-GC integrated with Pd-SnO$_2$ NRs can detect 1 ppm of H$_2$, as a lower detection limit, at a low operating temperature of 152 °C. Furthermore, when the breath hydrogen analyzer was exposed to a mixture of interfering gases, such as carbon dioxide, nitrogen, methane, and acetone, it was found to be capable of selectively detecting only H$_2$. We found that the Pd-SnO$_2$ NRs were superior to other semiconducting metal oxides that lack selectivity in H$_2$ detection. Our study reveals that the Pd-SnO$_2$ NRs integrated into the mini-GC device can be utilized in breath hydrogen analyzers to rapidly and accurately detect hydrogen due to its high selectivity and sensitivity.

Keywords: breath hydrogen analyzer; gas sensor; Pd-coated SnO$_2$ nanorods; gas chromatography; selectivity

1. Introduction

Humans are hosts to over 1000 species of microbes [1] that are responsible for human health and disease [2]. Important and promising studies have identified the effects of the human microbiome on disease conditions, such as obesity [3,4], diabetes [5,6], irritable bowel syndrome [7,8], fatty liver [9], and many others [10,11]. The majority of the microbes in the body inhabit the gastrointestinal tract, giving a chance for these organisms to influence metabolism, immunity, and digestion [12]. It is known that the gastrointestinal tract produces various gases, such as hydrogen, carbon dioxide, methane, and hydrogen sulfide, as the products of intestinal microbial metabolism, colonization, and subsequent fermentation [12]. Most of the gases are absorbed through the lining of the large intestine into the bloodstream. Then, the gases are transported to the lungs via the bloodstream where they are exchanged into the airways of the lungs and exhaled [13].

The source of H$_2$ in the breath can be from the bacterial fermentation of carbohydrates in the bowel caused by gastrointestinal diseases. Patients with gastrointestinal disorders have more aggressive fermentation, which results in premature and excessive amounts of H$_2$ due to inordinate microbial colonization [14]. The phenomenon is known as small intestinal bacterial overgrowth (SIBO). Therefore, some symptoms of irritable bowel syndrome (IBS) can be described by SIBO, and it can be diagnosed by the hydrogen breath test. However, the hydrogen breath test with lactulose can only diagnose one-third of the patients with SIBO, and the glucose hydrogen breath test is well-known to be highly specific for SIBO diagnoses [14]. On the other hand, some patients with IBS produce gases, such

as methane and hydrogen sulfide with or without hydrogen. In particular, patients with constipation may have higher methane contents, whereas patients with diarrhea, such as those with ulcerative colitis and Crohn's disease, may have higher hydrogen content [14,15]. Thus, hydrogen and methane have the potential for use as biomarkers for diarrhea and constipation, respectively. Accordingly, hydrogen breath tests can be useful for diagnosing many gastroenterological disorders, such as lactose and fructose malabsorption [16], celiac disease [10], Crohn's disease, and ulcerative colitis [15].

Relatively accurate hydrogen concentration measurements in the breath can be realized using various instrumentation. Nielsen et al. first introduced chromatographic techniques for quantitatively measuring small amounts of H_2 and CH_4 in breath samples and applied this method to humans [17,18]. Based on Nielsen's approach, various detectors, such as gas chromatography (GC) integrated with solid-state sensors [15,19,20], an infrared sensor combined with an electrochemical sensor [21], and a pulsed-discharge helium ionization detector (PHID) coupled with GC [22,23], have been developed to measure H_2 and CH_4 in breath samples. Among them, Raman gas spectroscopy exhibits excellent chemical selectivity for various gases in complex mixtures [24,25]. However, most instruments for measuring breath hydrogen and methane are still expensive, not portable, and complex. It is, therefore, necessary to develop such instruments with inexpensive and miniaturized components and simplified detection procedures.

To develop a compact analyzer, it is critical to find high-performance sensing materials. Metal-oxide-semiconductor (MOS) based sensors can be used in a portable gas sensing system owing to several of their advantages, including high-sensitivity, fast response-time, compact size, and low cost. Specifically, it is easy to fabricate nanostructures to achieve high-sensitivity [26–31]. Many metal oxides, including SnO_2, ZnO, WO_3, TiO_2, In_2O_3, Nb_2O_5, FeO, NiO, Fe_2O_3, Ga_2O_3, MoO_3, Sb_2O_5, and V_2O_5, which exhibit a large variation in electrical resistance after exposure to hydrogen gas, have been investigated for use as hydrogen sensing materials in MOS [27,28]. Among the MOS sensing materials, SnO_2 has been widely used to detect H_2 because of its high-sensitivity [29]. Additionally, the hydrogen sensing performance of SnO_2 has been further enhanced by utilizing noble metals [30]. Notably, Pd is the most widely used metal for enhancing the sensing response of H_2 and decreasing the optimal working temperature [29,31]. However, most studies conducted on SnO_2-based hydrogen sensors have focused on detecting H_2 leakage during storage/transport/use and detecting H_2 dissolved in transformer oil; it has been found that the lowest detection limit is 4% for the former [32] and 100–500 ppm for the latter [33]. Both results are much higher than that of the concentration of breath hydrogen. The concentration of breath hydrogen is approximately 2 ppm [34] in healthy people and greater than 10 ppm [35] in patients with carbohydrate malabsorption. Therefore, research concerning SnO_2-based hydrogen sensors for the application of the exhaled breath analyzer is valuable. Furthermore, selective detection of target gas in a mixed gas is a significant obstacle in MOS sensors such as those based on SnO_2. Consequently, it is necessary to adopt GC to resolve the selectivity issue of MOS sensors.

In this work, we investigated the sensing performance of Pd-coated SnO_2 nanorod arrays (NRs) integrated with a miniaturized GC column to detect H_2 selectively for an application of a breath hydrogen analyzer. The H_2 sensing properties of the breath analyzer were investigated based on the sensing responses at various concentrations of H_2 (1–100 ppm). The selectivity of the breath analyzer for detecting H_2 was studied by exposing it to mixtures of gases, such as H_2, CO_2, N_2, CH_4, and CH_3COCH_3. We compared the Pd-SnO_2 NRs with ZnO nanoparticles, which lack selectivity in detecting H_2. We also discuss the humidity effect on the sensing performance of the breath hydrogen analyzer.

2. Materials and Methods

2.1. Fabrication and Characterization

The vertically oriented SnO_2 nanorods (NRs) were synthesized on an Al_2O_3 substrate (5×2.5 mm^2) by the glancing angle deposition method (GLAD) using an electron-beam

evaporator. In the GLAD method, by adjusting the incident angle of the vapor flux and the substrate rotation speed, vertically ordered nanorod arrays with high-density, as well as nanorods of uniform diameter and length can be fabricated [31]. Before the synthesis of the NRs, a DC sputtering system was used to fabricate interdigitated electrodes (Pt, 100 nm in thickness) and a heater (Pt, 600 nm in thickness) on the top and bottom of the alumina substrate, respectively. The patterned alumina substrate was loaded onto the sample holder in the sputtering system. SnO_2 granules (99.99% Kojundo Chemical Laboratory Co., Ltd., Saitama, Japan) that had an average size of 3 mm were placed in a crucible that was located 50 cm below the sample holder. The sample holder was tilted at 80° and rotated at a speed of 15 rpm during the growth of the SnO_2 NRs. Electron-beam evaporation was performed with a 1 Å/s deposition rate at a base pressure of 5.0×10^{-6} Torr. The as-deposited sample was annealed at 550 °C for 2 h. After the synthesis of the SnO_2 NRs, a 5 nm Pd layer was deposited on the annealed SnO_2 NRs with a power of 20 W in an Ar atmosphere using an ultra-high vacuum DC magnetron sputtering system. The base pressure was 4.1×10^{-8} Torr, and the deposition process was conducted at a pressure of less than 2.3×10^{-3} Torr with an Ar flow rate of 34 SCCM. A high-purity Pd target (4N) was used, and the Pd deposition rate was ~4.7 Å/s at room-temperature. The morphology and the compositional analysis of the $Pd-SnO_2$ NRs were examined by a field emission scanning electron microscope (FE-SEM, JSM-7001F, JEOL Ltd., Tokyo, Japan) equipped with an energy dispersive X-ray spectrometer (FE-SEM-EDX, JSM-7001F, JEOL Ltd., Tokyo, Japan).

ZnO NPs also were prepared by using a wet chemical method in order to compare the sensing performance of the $Pd-SnO_2$ NRs to the ZnO nanoparticles (NPs) recently developed by our group [36]. The synthesized ZnO NPs were dispersed in methanol. More details of the synthesis method for ZnO NPs are available in our previous work [36]. The sensor was fabricated by dropping the ZnO NPs solution onto the patterned Al_2O_3 substrate and heat-treated at 600 °C for 30 min.

2.2. Gas Sensing Test

We conducted an H_2 sensing test using miniaturized gas chromatography (mini-GC). Figure 1 shows the mini-GC that had the dimensions of 8 cm × 13 cm × 16 cm. The mini-GC gas analyzer consisted of a sensor based on $Pd-SnO_2$ NRs, a packed column, a sampling loop (1 mL), a mini-sized pump, and three solenoid valves. The sampling volumes of the gases were limited to 1 mL. We use dry air as a carrier gas to continuously supply oxygen ions to the surface of the $Pd-SnO_2$ NRs because the gas sensing mechanism of metal-oxide semiconducting materials, such as SnO_2, is based on changes in the thickness of the depletion layer by oxygen ion adsorption onto the surface. The flow rate of the carrier gas affects the sensing response because the sensing material requires a certain amount of time to react with the gas. Herein, the flow rate of the carrier gas was adjusted using a flow control valve and maintained 30 SCCM for analysis. Prior to injection into the GC system, the ambient air was passed through a filter filled with silica gel to remove any moisture.

We chose a packed GC column because of its huge surface area, low cost, and good operability at room-temperature [37]. The packed column was filled with a packing material coated with the stationary phase (Isenlab Inc., Seongnam-si, South Korea) and the column's inner diameter was 0.15 cm. The length of the column was adjusted to 30 cm to achieve a short retention time of the target gas. Gas separation occurs during the mixture of gas passing through the column, due to the differing interaction strengths between the various gas molecules and the stationary phase. The interaction strength is related to the polarity and size of the gas molecules and the stationary phase of the packed column was weakly polar. Thus, small non-polar gases, such as H_2, N_2, and CO_2, were quickly released from the column owing to their weak interactions while larger polar gases, such as acetone, were slowly released owing to their strong interactions with the stationary phase.
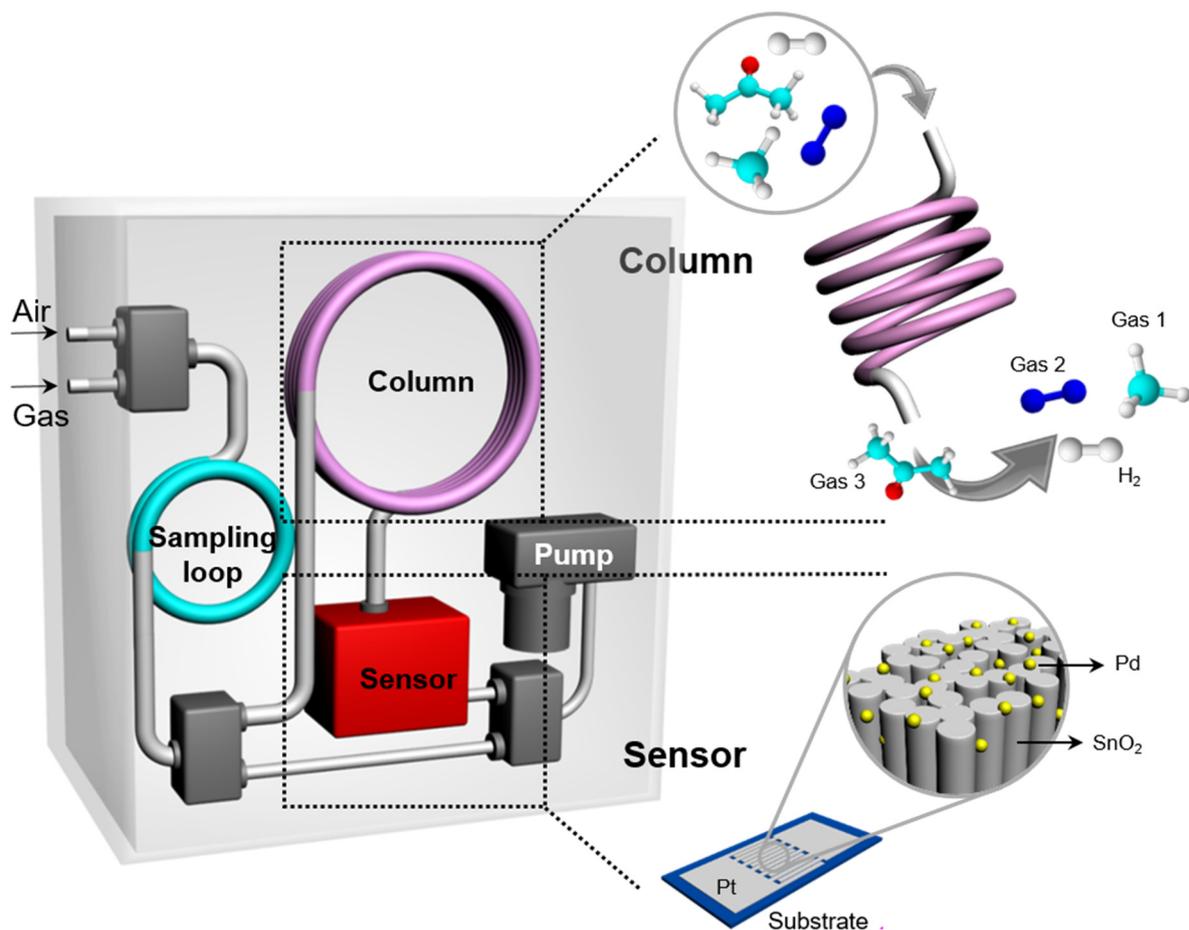
Figure 1. Schematic illustration of a hydrogen analyzer using a miniaturized gas chromatography (mini-GC).

The sensing process of the breath hydrogen analyzer based on Pd-SnO$_2$ NRs is described as follows. First, a 1 mL mixture of the target gas and ambient air was used to fill the sampling loop for 100 s without pre-concentration. Subsequently, the sampled gas was injected into the packed column and the components of the gas were separated by the interaction between the stationary phase and gas molecules as they passed through in the packed column. The temperature of the column was maintained at room-temperature (30 °C) by controlling the thermostat. The target gas that passed through the column was detected by the Pd-SnO$_2$ NR or ZnO NPs. To optimize the working temperature of the sensor, the sensor response was tested at various temperatures, i.e., 25, 80, 115, 139, 152, 165, 178, and 191 °C. The ability of the analyzer to sense the presence of H$_2$ was checked at various concentrations of H$_2$ in the range of 1–100 ppm at the optimal working temperature. The hydrogen concentration was controlled by changing the mixing ratio between highly concentrated hydrogen in an airbase and synthetic air using a mass flow controller. The selectivity of the mini-GC system for H$_2$ was investigated by measuring its responses when exposed to various gases, including H$_2$, CO$_2$, N$_2$, CH$_4$, and CH$_3$COCH$_3$ and comparing its responses to those of ZnO nanoparticles.

The sensing performance was evaluated based on the resistance of the sensor, and the resistance obtained in the gas analyzer was converted to a sensor signal ($\log(R)$). The change in the sensing signal of the samples was defined as $\Delta \log(R)$ [38].

$$\Delta \log(R) = \log(R)_{max} - \log(R)_{min}, \tag{1}$$

where $\log(R)_{max}$ and $\log(R)_{min}$ are the maximum and minimum values before and after exposure to H$_2$, respectively.

2.3. Gas Sensing Mechanism

Figure 2 shows the underlying sensing mechanism of the Pd-SnO$_2$ NRs for the detection of H$_2$. When the Pd-SnO$_2$ NRs were exposed to air, oxygen molecules in the air were adsorbed on the surfaces of the Pd nanoparticles (NPs) and the SnO$_2$ NR. The adsorbed oxygen molecules took the electrons from the conduction band of the SnO$_2$ NR and formed anionic oxygen species (O$_2^-$, O$^-$, and O^{2-}) depending on the working temperature. At temperatures greater than 150 °C, O$^-$ and O^{2-} were chemisorbed [39,40]. O$_2^-$ commonly is chemisorbed at low temperatures (T < 150 °C) [41]. Since the working temperature of SnO$_2$ NR was in the range of >150 °C, the O$^-$, and O^{2-} ions were adsorbed on the surface of the SnO$_2$ NRs. In addition, oxygen molecules can be adsorbed on the surface of the Pd NPs and be easily dissociated into O$^-$ ions due to the spillover effect of the Pd metal [42]. Due to the higher work function of Pd metal (Φ_{Pd} = 5.12 eV) compared to that of SnO$_2$ (Φ_{SnO_2} = 4.9 eV), a Schottky barrier was formed at the interface between Pd and SnO$_2$ [43], and the electrons that were associated with SnO$_2$ were transferred to the Pd metal. This resulted in the enhanced dissociation of oxygen molecules into O$^-$ ions on the surface of the Pd NPs, and these ions easily diffused into the surface vacancies of the SnO$_2$ NR. Consequently, thicker electron depletion layers were formed at the interface between the Pd NPs and the SnO$_2$ NR. This infers that a greater number of reactive sites for H$_2$ was produced on the surface of the Pd-SnO$_2$ NR.

$$H_2(\text{gas}) \rightarrow 2H(\text{adsorb}) \tag{2}$$

$$2H(\text{adsorb}) + O^-(\text{adsorb}) \rightarrow H_2O + e^- \tag{3}$$
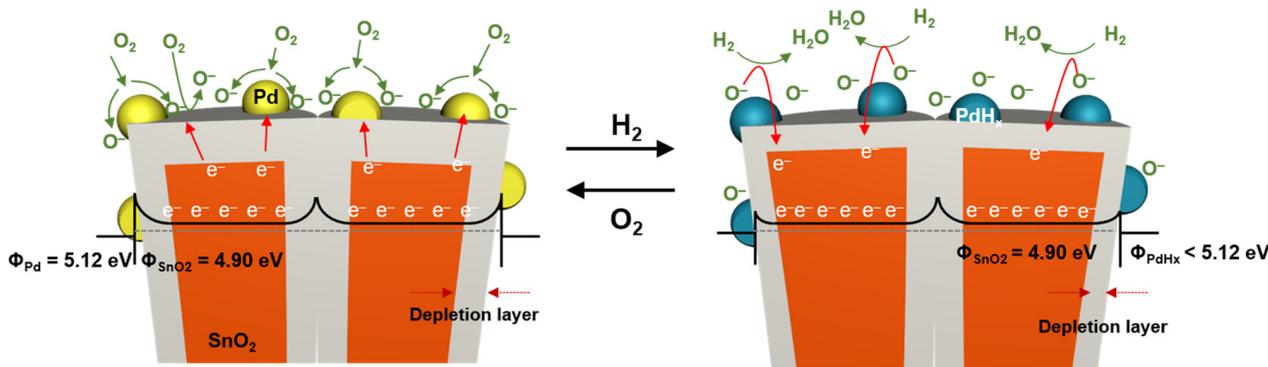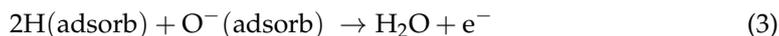
Figure 2. Schematic image of the sensing reaction mechanism of Pd-coated SnO$_2$ NR arrays in air and hydrogen.

When the Pd-coated SnO$_2$ NRs were exposed to H$_2$, the H$_2$ molecules decomposed into hydrogen atoms (Equation (2)). The dissociated hydrogen atoms change Pd into PdH$_x$ [44], leading to a reduction in the work function of Pd ($\Phi_{Pd} > \Phi_{PdHx}$) and a decrease in the height of the Schottky barrier. In addition, the hydrogen atoms reacted with a large number of the O$^-$ ions (Equation (3)) that were formed at the initial state of the surface of the sample. According to the reaction in Equation (3), electrons are returned to the conduction band of SnO$_2$. Therefore, the thickness of the depletion layer is reduced, thereby decreasing the resistance of the Pd-SnO$_2$ NR.

3. Results and Discussion

Figure 3 shows an image of the as-synthesized Pd-SnO$_2$ NR. Figure 3a,b show the top and cross-sectional views, respectively, of the SEM images of the Pd-SnO$_2$ NRs grown on the Al$_2$O$_3$ substrate. Figure 3c is a magnified view of Figure 3a. The SEM image (top-view) shows that the SnO$_2$ NRs predominantly were clustered and located randomly. The diameters of the NR clusters were 40–200 nm, and the distances between the adjacent clustered NR ranged from 5 to 40 nm. Figure 3c shows that the clusters consisted of small

grains (~40 nm). This indicated that the diameter of the SnO_2 NR was about 40 nm. The cross-sectional-view SEM image of Figure 3b shows that all of the SnO_2 NRs were aligned vertically with respect to the substrate, and the average height of the SnO_2 NR was 250 nm. Figure 3d shows the EDX mapping images of the cross-sectional-view SEM image, and it shows the SnO_2 NR on the Al_2O_3 substrate. The deposited Pd nanoparticles were dispersed uniformly on the top and side surfaces of the SnO_2 NRs.
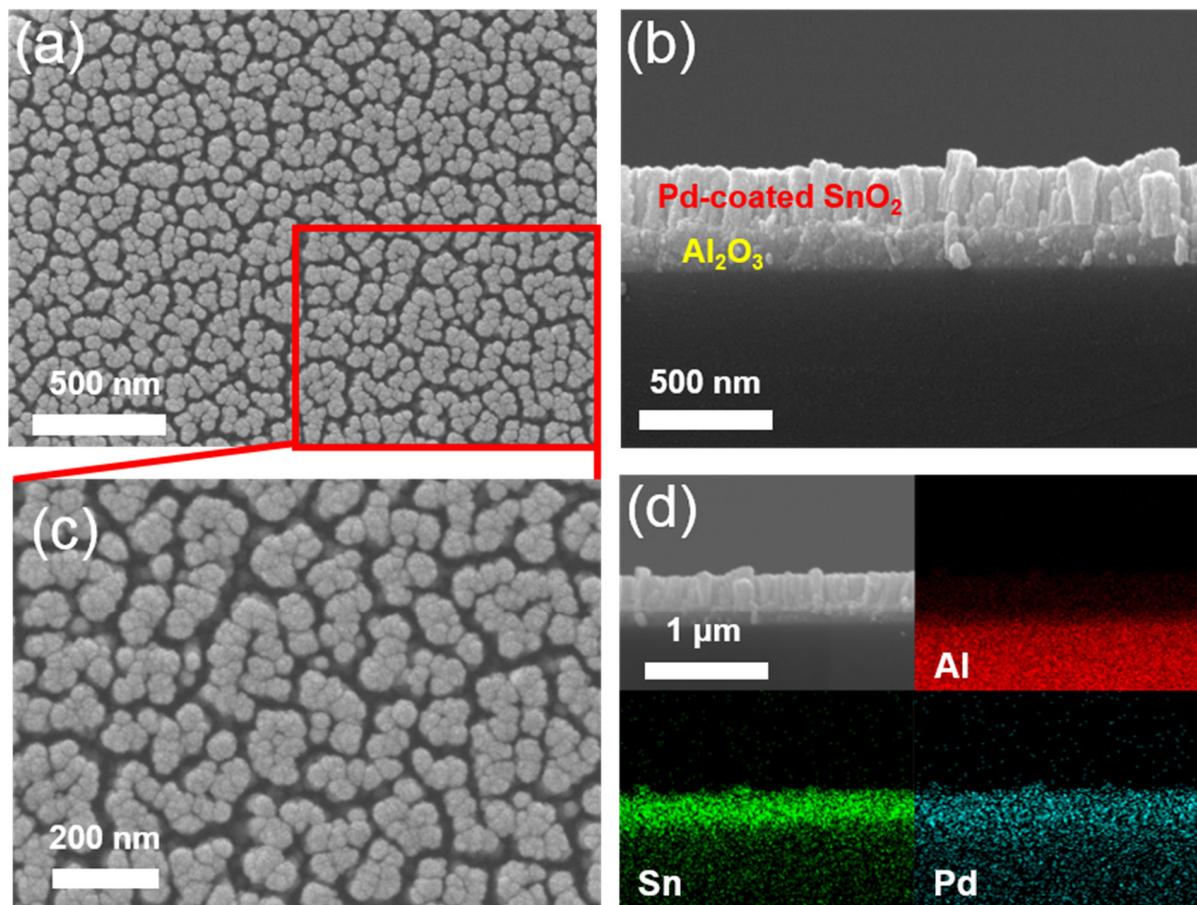
Figure 3. (**a**) Top-view SEM images of the Pd-coated SnO_2 NR arrays; (**b**) cross-view SEM images of the Pd-coated SnO_2 NR arrays; (**c**) a magnified view of (**a**); (**d**) SEM image depicting the analyzed region and the EDS elemental color mapping images for Al, Sn, and Pd.

The sensing properties of Pd-SnO_2 NRs in the mini-GC system were tested for various H_2 contents. Figure 4a shows the H_2 sensing response of the Pd-SnO_2 NRs integrated with mini-GC to 100 ppm of H_2 as a function of operating temperature. The optimal working temperature of the sensor was 152 °C. The response increased and reached a maximum at 152 °C, after which it decreased with increasing temperature. These results were due to the competition between the slow kinetics at lower temperatures and improved desorption at higher temperatures.

Figure 4b shows the variation with time of the sensor signal (log(R)) of the Pd-SnO_2 NRs integrated with mini-GC for various H_2 concentrations (1–100 ppm) at the optimal working temperature of 152 °C. The inset of Figure 4b shows a magnified plot of the main figure for low H_2 concentrations (1–10 ppm). When H_2 was present, a noticeable peak occurred at about 10 s for various concentrations of H_2. We found that the Pd-SnO_2 NRs integrated with mini-GC was capable of detecting 1 ppm of H_2, as indicated in the inset of Figure 4b. As the concentration of H_2 increased, the height of a peak became larger. The change in the resistance was attributed to the sensing reaction of Pd-SnO_2 NRs with H_2, as described in Figure 2. As the H_2 concentration increased, the thickness of the depletion

layer becomes thinner due to the reaction of the O_2^- and O^- ions with the hydrogen atoms that decomposed on the surfaces of the SnO_2 NRs and Pd nanoparticles. However, the change in the resistance of the Pd-SnO_2 NRs was found to be changed without H_2 in ambient air. Figure 4c shows the change in the sensing signal of the Pd-SnO_2 NRs integrated with a mini-GC column for various H_2 concentrations at 152 °C. The change in the sensing signal was defined as $\Delta \log(R)$ according to Equation (1), and an increase was observed with an increase in H_2 concentration for the various H_2 concentrations (1–100 ppm) at 152 °C.
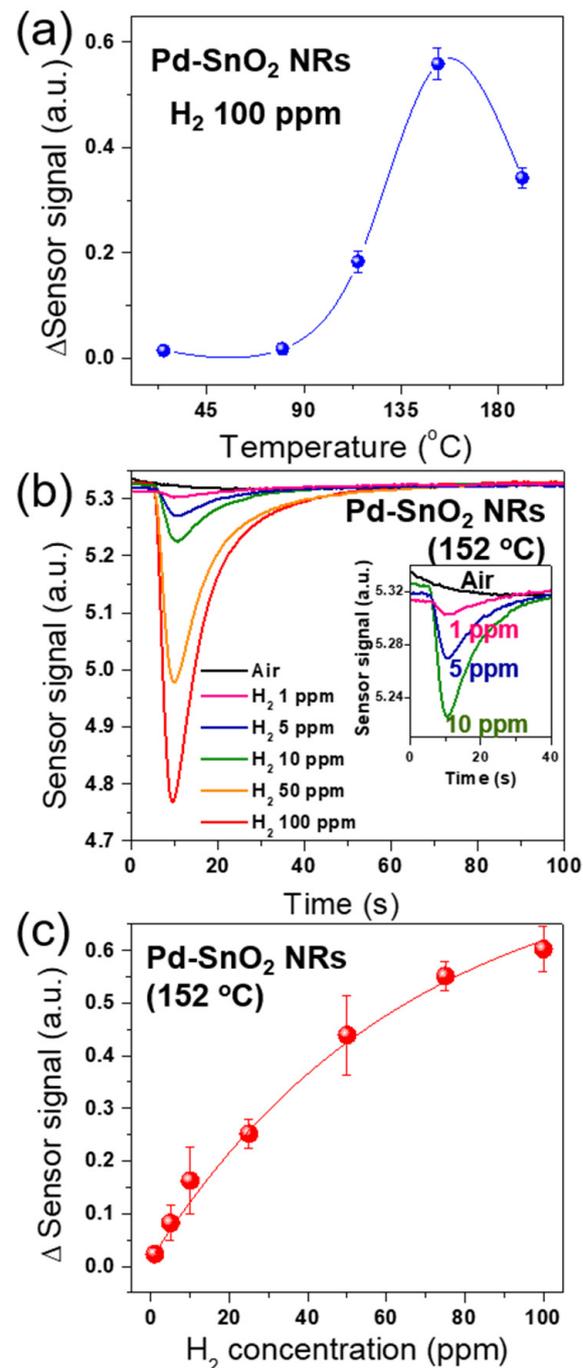
Figure 4. Sensing properties of the Pd-coated SnO_2 NR arrays using the mini-GC: (**a**) sensing response (Δ Sensor signal) to 100 ppm hydrogen as a function of operating temperature; (**b**) sensor signals of the Pd-coated SnO_2 NR arrays to various H_2 concentrations (1–100 ppm) at 152 °C (Inset: the cases of low H_2 concentration (1–10 ppm)); (**c**) sensing response as a function of H_2 concentrations at 152 °C.

In order to investigate the H_2 selectivity of the Pd-SnO$_2$ NRs integrated with mini-GC, we conducted measurements of the sensing signals for various gases in Pd-SnO$_2$ NRs and ZnO NPs integrated with mini-GC at their respective optimal operating temperatures. Figure 5a shows the sensor signals for H_2, CO_2, and CH_3COCO_3 in the ZnO NPs integrated with mini-GC. Figure 5b shows sensor signals for air, H_2, N_2, CO_2, CH_4, and CH_3COCH_3 in the Pd-SnO$_2$ NRs integrated with mini-GC.
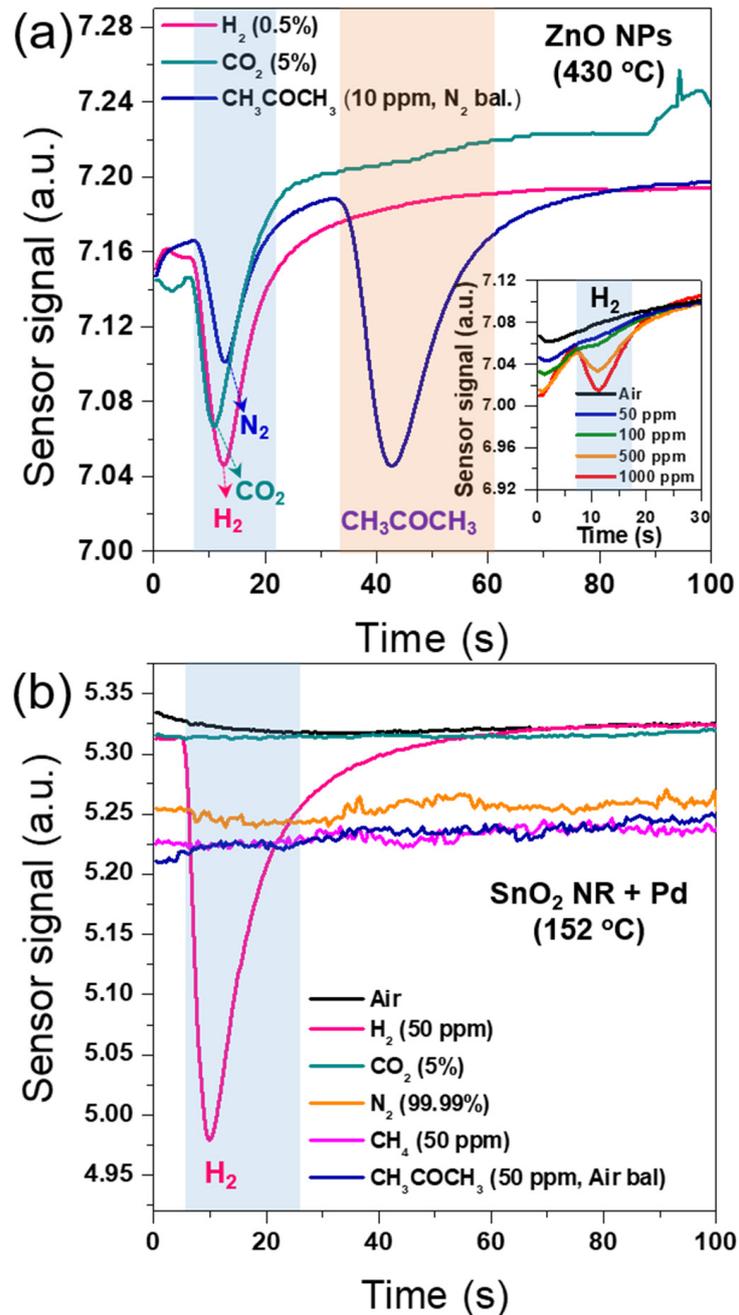
Figure 5. (**a**) Sensor signals for H_2, CO_2, and CH_3COCO_3 in the mini-GC integrated with ZnO nanoparticles (Inset: the cases of low H_2 concentration (50–1000 ppm); (**b**) sensor signals for air, H_2, N_2, CO_2, CH_4, and CH_3COCH_3 in the mini-GC integrated with Pd-coated SnO$_2$ NR arrays.

In Figure 5a, the sensor signals of the ZnO NPs integrated with mini-GC were obtained upon exposure to 0.5% H_2 in synthetic air, 5% CO_2, and 10 ppm CH_3COCH_3 in N_2. The sensing measurements were performed at the optimal operating temperature of 430 °C for the ZnO NPs integrated with mini-GC (see Figure S1 in Supplementary Material). The two peaks that occurred at about 13 s were observed in the sensor signals for 0.5% H_2 and 5% CO_2, corresponding to the detection of H_2 and CO_2, respectively. The curve for 10 ppm acetone in N_2 had two peaks, one at 13 s and one at 42 s. The first and second peak represented the emission of N_2 and acetone, respectively. The corresponding time of the second peak was consistent with the detection time of air-balanced acetone observed in our previous work [38]. In our mini-GC system, the target gas can be separated from the mixture gas due to the different strength of interaction between the gas molecules and the stationary phase in the packed column. The stationary phase in a GC column has a weak polarity. Therefore, due to their weak interaction, non-polar gases, such as H_2, N_2, and CO_2, are released rapidly from the GC column. However, CH_3COCH_3, which is a polar gas, was released slowly. In this regard, H_2 is very difficult to detect selectively in the mixture of N_2 and CO_2 in the ZnO NPs integrated with mini-GC.

Figure 5b shows the sensing signals when the Pd-SnO$_2$ NRs integrated with the mini-GC was tested at 152 °C upon exposure to various gases, such as ambient air, 50 ppm H_2, 5% CO_2, 99.99% N_2, 50 ppm CH_4, and 50 ppm CH_3COCH_3 in air. Only the sensor signal of 50 ppm H_2 had a noticeably large peak at about 10 s. There was no change in the resistance of the sensor when exposed to the other gases, because an operating temperature of 152 °C is too low to detect these gases, including carbon oxides and hydrocarbons. The results implied that the Pd-SnO$_2$ NRs integrated with the mini-GC had high selectivity for H_2 at 152 °C. According to the definition of the "Δ Sensor signal", the sensing response of the Pd-SnO$_2$ NRs to 50 ppm H_2 was estimated to be about 0.33 (Figure 5b), which was higher than the sensing response of 0.11 when the ZnO NPs were exposed to 0.5% H_2 (Figure 5a). In addition, the hydrogen sensing peak of the ZnO NPs at 50 ppm H_2 was difficult to distinguish from the baseline, as shown in the inset of Figure 5a. This indicates that the ZnO NPs cannot detect low hydrogen concentrations of <50 ppm. Therefore, the sensing performance of the Pd-SnO$_2$ NRs toward H_2 was shown to be significantly better than that of the ZnO NPs. The superior H_2 sensing property of the Pd-SnO$_2$ NRs was attributed to the synergistic effect of the catalyst and the height of the Schottky barrier, as described in Figure 2. Accordingly, the Pd-SnO$_2$ NRs integrated with the mini-GC had high selectivity and sensitivity for the detection of H_2 at the relatively-low working temperature of 152 °C.

We investigated the H_2 sensing performance of Pd-SnO$_2$ NRs integrated with mini-GC in a humid condition. Figure 6 shows the change of the sensor's signal for various H_2 concentrations (1–100 ppm) at the highly humid condition of 90% relative humidity (RH) at 152 °C. All of the sensor signals for the different H_2 concentrations had a peak at ~10 s, corresponding the detection of H_2. The intensity of the peaks became larger as the H_2 concentration was increased. These results were consistent with those obtained for H_2 in dry air (Figure 4a). The inset of Figure 6 shows the Δ Sensor signal of the Pd-SnO$_2$ NRs to various H_2 concentrations in dry and humid (90% RH) air. The results indicated that the sensitivity of the Pd-SnO$_2$ NRs was decreased at 90% RH, but the sensor was able to detect H_2 concentrations as low as 5 ppm at 90% RH.
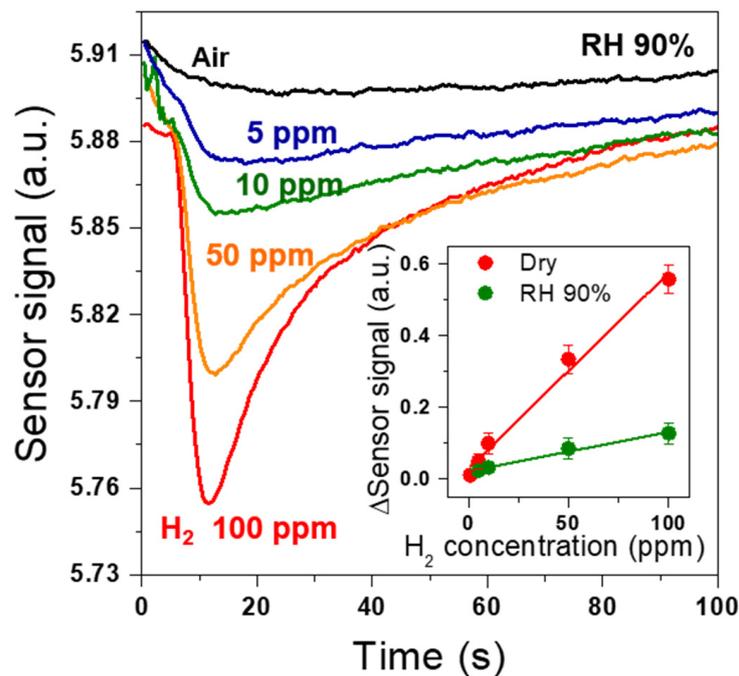
Figure 6. Sensor signals of Pd-coated SnO$_2$ NR arrays for various H$_2$ concentrations (5–100 ppm) at 90% RH and 152 °C; (inset) sensing response (Δ Sensor signal) with increasing H$_2$ concentration in dry and 90% RH air.

To demonstrate the potential of the Pd-SnO$_2$ NRs sensor integrated with a mini-GC device for use in real-time monitoring, the performance of the manufactured sensing measurement system was evaluated using standard hydrogen gas. To determine the hydrogen content detected, the relation function between the Δ Sensor signal and H$_2$ concentration (Figure 4c) was utilized. Figure 7a–f shows the analysis process for measuring the concentration of the injected standard hydrogen gas. The measurement instructions were displayed on the front panel. After pressing the start button, a test gas of 10 ppm hydrogen was injected (Figure 7b). Gas sampling was performed for 20 s, and ambient air was used as the carrier gas (Figure 7c). After an analysis time of 100 s (Figure 7d,e), the system indicated that the concentration of hydrogen detected was 10.53 ppm (Figure 7f). Figure 8a–f shows the same analysis procedure for measuring the concentration of the hydrogen gas in exhaled breath; the results indicated that 9.66 ppm hydrogen was dissolved in the breath exhaled by the tester. This is consistent with several reports [45–47] that fasting basal hydrogen concentration in normal people's breath is 8–10 ppm. According to the results, our study demonstrated that the manufactured hydrogen gas analyzer, which consisted of a Pd-SnO$_2$ NRs sensor and a mini-GC device, can rapidly and accurately detect hydrogen within 100 s; consequently, it should be utilized in analyzers for breath hydrogen testing.
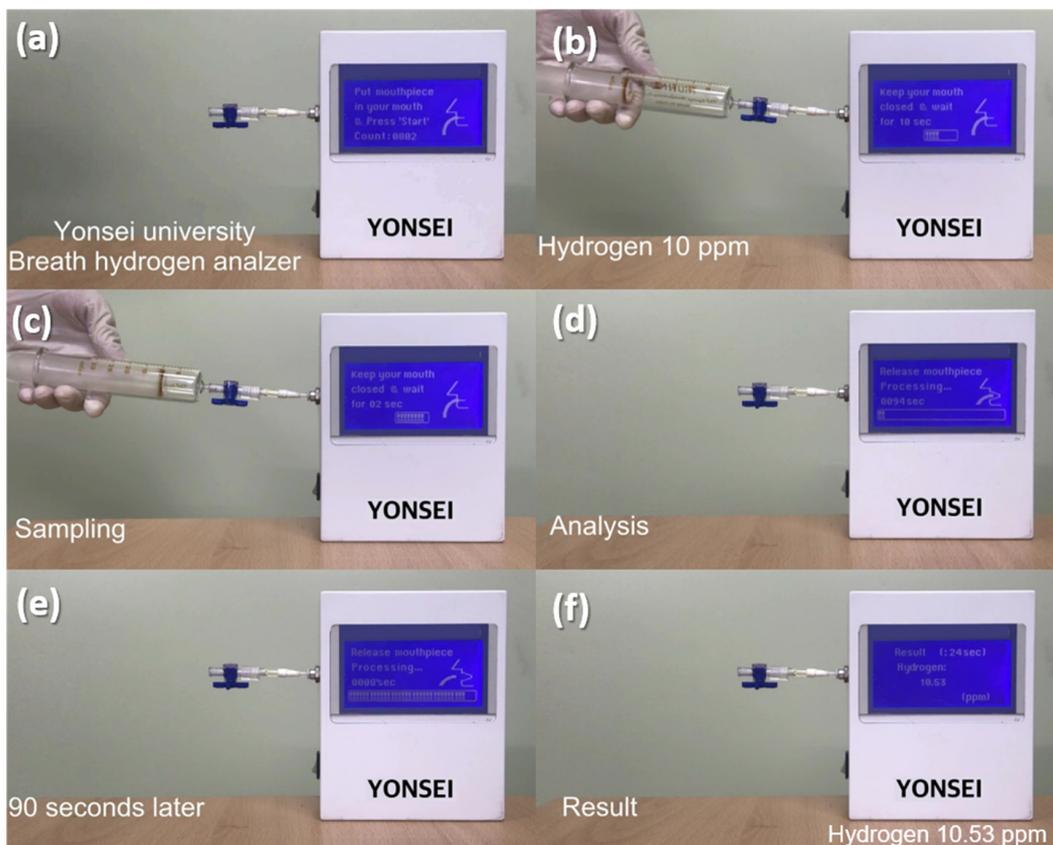
Figure 7. Real-time hydrogen gas sensing test via the manufactured hydrogen gas analyzer, consisting of Pd-coated SnO$_2$ NR sensor and mini-GC, using 10 ppm of standard hydrogen gas. (**a**) Put mouthpiece in you mouth and Press the start button, (**b**) Injection of a standard test gas of 10 ppm hydrogen, (**c**) Gas sampling for 20 s, (**d**) Starting gas analysis, (**e**) After 90 s of gas analysis, and (**f**) Display of the gas analysis result.
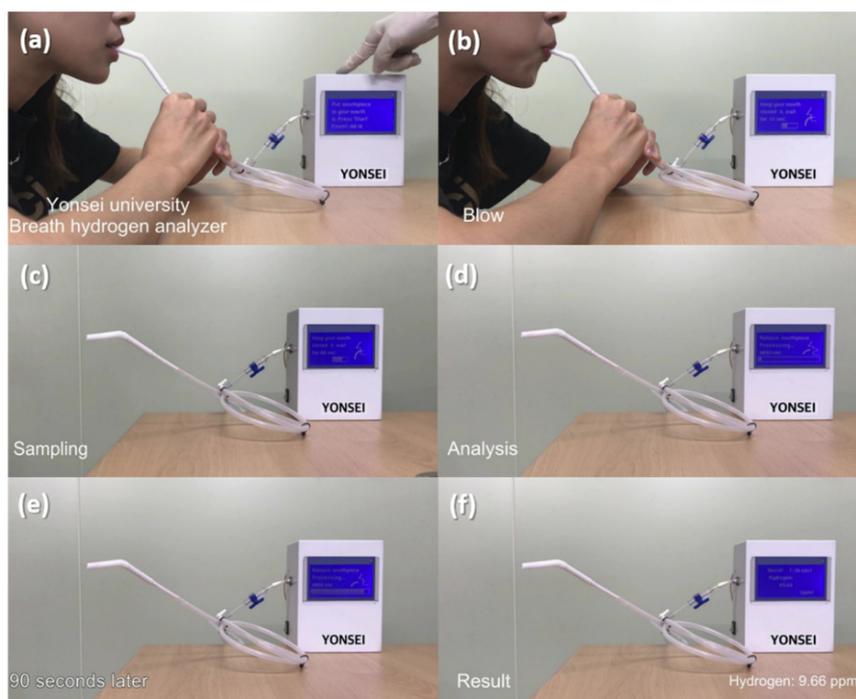
Figure 8. Real-time hydrogen gas sensing test via the manufactured hydrogen gas analyzer, consisting

of Pd-coated SnO_2 NR sensor and mini-GC, using tester's exhaled breath. (**a**) Pressing the start button, (**b**) Blowing the exhaled breath for 12 s, (**c**) Gas sampling for 20 s, (**d**) Starting gas analysis, (**e**) After 90 s of gas analysis, and (**f**) Display of the gas analysis result.

4. Conclusions

We studied the sensing performance of a breath hydrogen analyzer based on a Pd-coated SnO_2 nanorods (Pd-SnO_2 NRs) integrated with miniaturized gas chromatography (GC) column. We found that the breath hydrogen analyzer was capable of measuring H_2 over a wide range of concentrations (1–100 ppm), within 100 s, at an optimal operating temperature of 152 °C. We also found that the Pd-SnO_2 NRs could detect H_2 selectively in mixtures of interfering gases, such as CO_2, N_2, CH_4, and CH_3COCH_3. The higher performance of the Pd-SnO_2 NRs compare to the ZnO NPs for sensing H_2 was explained based on the catalytic effect and the reduction in the height of the Schottky barrier. Accordingly, we have summarized the meaningful advantages of our device as follows: smaller dimension ($8 \times 13 \times 16$ cm^3), lower cost, lower power (12 V), smaller sampling volume (1 mL), lower operating temperature (152 °C), lower detection limit (1 ppm), and detection time (10 s). This study is a first report on a prototype of a portable and compact breath-hydrogen-analyzer device, based on MOS sensors, such as Pd-SnO_2 NRs. The potential of the device as a breath hydrogen analyzer has been demonstrated by evaluating it with breath exhaled by a real human. More importantly, the device can selectively and sensitively detect trace amounts of hydrogen mixed in various VOC gases exhaled by humans.

Supplementary Materials: The following supporting information can be downloaded at: https://www.mdpi.com/article/10.3390/s22052056/s1, Figure S1: Δ Sensor signal of ZnO nanoparticles integrated into the mini-GC to 5000 ppm (0.5%) hydrogen as a function of operating temperature.

Author Contributions: Conceptualization, H.J. and W.L.; investigation, H.J. and J.H.; methodology, H.J., J.H. and Y.-S.C.; validation, Y.-S.C. and H.-S.L.; writing—original draft preparation, H.J. and H.-S.L.; writing—review and editing, H.-S.L.; supervision, W.L.; project administration, W.L.; funding acquisition, W.L. All authors have read and agreed to the published version of the manuscript.

Institutional Review Board Statement: Not applicable.

Informed Consent Statement: Not applicable.

Data Availability Statement: Not applicable.

Conflicts of Interest: The authors declare no conflict of interest.

References

1. Eckburg, P.B.; Bik, E.M.; Bernstein, C.N.; Purdom, E.; Dethlefsen, L.; Sargent, M.; Gill, S.R.; Nelson, K.E.; Relman, D.A. Diversity of the human intestinal microbial flora. *Science* **2005**, *308*, 1635. [CrossRef] [PubMed]
2. Dukowicz, A.C.; Lacy, B.E.; Levine, G.M. Small intestinal bacterial overgrowth: A comprehensive review. *Gastroenterol. Hepatol.* **2007**, *3*, 112.
3. Turnbaugh, P.J.; Ley, R.E.; Mahowald, M.A.; Magrini, V.; Mardis, E.R.; Gordon, J.I. An obesity-associated gut microbiome with increased capacity for energy harvest. *Nature* **2006**, *444*, 1027. [CrossRef] [PubMed]
4. Samuel, B.S.; Gordon, J.I. A humanized gnotobiotic mouse model of host-archaeal-bacterial mutualism. *Proc. Natl. Acad. Sci. USA* **2006**, *103*, 10011–10016. [CrossRef]

5. Cani, P.D.; Bibiloni, R.; Knauf, C.; Wagnet, A.; Neyrinck, A.M.; Delzenne, N.M.; Burcelin, R. Changes in gut microbiota control metabolic endotoxemia-induced inflammation in high-fat diet-induced obesity and diabetes in mice. *Diabetes* **2008**, *57*, 1470. [CrossRef]

6. Musso, G.; Gambino, R.; Cassader, M. Interactions between gut microbiota and host metabolism predisposing to obesity and diabetes. *Annu. Rev. Med.* **2011**, *62*, 361. [CrossRef]

7. Kerckhoffs, A.P.M.; Samsom, M.; Rest, M.E.; Vogel, J.; Knol, J.; Amor, K.B.; Akkermans, L.M.A. Lower Bifidobacteria counts in both duodenal mucosa-associated and fecal microbiota in irritable bowel syndrome patients. *World J. Gastroenterol.* **2009**, *15*, 2887. [CrossRef]

8. Skoog, S.M.; Bharucha, A.E.; Zinsmeister, A.R. Comperison of breath testing with fructose and high fructose corn syrups in health and IBS. *Neurogastroenterol. Motil.* **2008**, *20*, 505–511. [CrossRef]

9. Fialho, A.; Fialho, A.; Thota, P.; McCullough, A.J.; Shen, B. Small intestinal bacterial overgrowth is associated with non-alcoholic fatty liver disease. *J. Gastrointest. Liver Dis.* **2016**, *25*, 159–165. [CrossRef]

10. Corazza, G.R.; Strocchi, A.; Gasbarrini, G. Fasting breath hydrogen in celiac disease. *Gastroenterology* **1987**, *93*, 53–58. [CrossRef]

11. Casellas, F.; Malagelada, J.R. Applicability of short hydrogen breath test for screening of lactose malabsorption. *Dig. Dis. Sci.* **2003**, *48*, 1333–1338. [CrossRef] [PubMed]

12. Pimentel, M.; Mathur, R.; Chang, C. Gas and the microbiome. *Curr. Gastroenterol. Rep.* **2013**, *15*, 356. [CrossRef] [PubMed]

13. Rana, S.V.; Malik, A. Hydrogen breath test in gastrointestinal diseases. *Indian J. Clin. Biochem.* **2014**, *29*, 398–405. [CrossRef] [PubMed]

14. Ghoshal, U.C. How to interpret hydrogen breath tests. *J. Neurogastroenterol. Motil.* **2011**, *17*, 312–317. [CrossRef] [PubMed]

15. Pimentel, M.; Mayer, A.G.; Park, S.; Chow, E.J.; Hasan, A.; Kong, Y. Methane Production During Lactulose Breath Test Is Associated with Gastrointestinal Disease Presentation. *Dig. Dis. Sci.* **2003**, *48*, 86–92. [CrossRef]

16. Usai-Satta, P.; Oppia, F.; Lai, M.; Cabras, F. Hydrogen Breath Tests: Are They Really Useful in the Nutritional Management of Digestive Disease? *Nutrients* **2021**, *13*, 974. [CrossRef]

17. Nielsen, J.P. *Final Report, Contract No. 12-14-100-2628 (74)*; Western Regional Research Laboratory, U.S.D.A.: Albany, CA, USA, 1960.

18. Stefano, M.D.; Missanelli, A.; Miceli, E.; Strocchi, A.; Corazza, G.R. Hydrogen breath test in the diagnosis of lactose malabsorption: Accuracy of new versus conventional criteria. *J. Lab. Clin. Med.* **2004**, *144*, 313–318. [CrossRef]

19. Basseri, R.J.; Basseri, B.; Pimentel, M.; Chong, K.; Youdim, A.; Low, K.; Hwang, L.; Soffer, E.; Chang, C.; Mathur, R. Intestinal Methane Production in Obese Individuals Is Associated with a Higher Body Mass Index. *Gastroenterol. Hepatol.* **2012**, *8*, 22.

20. Mathur, R.; Amichai, M.; Chua, K.S.; Mirocha, J.; Barlow, G.M.; Pimentel, M. Methane and Hydrogen Positivity on Breath Test Is Associated With Greater Body Mass Index and Body Fat. *J. Clin. Endocrinol. Metab.* **2013**, *98*, E698–E702. [CrossRef]

21. de Lacy Costello, B.P.J.; Ledochowski, M.; Ratcliffe, N.M. The importance of methane breath testing: A review. *J. Breath Res.* **2013**, *7*, 024001. [CrossRef]

22. Ngai, A.K.Y.; Persijn, S.T.; von Busum, G.; Harren, F.J.M. Automatically tunable continuous-wave optical parametric oscillator for high-resolution spectroscopy and sensitive trace-gas detection. *Appl. Phys. B* **2006**, *85*, 173–180. [CrossRef]

23. Roberge, M.T.; Finley, J.W.; Lukaski, H.C.; Borgerding, A.L. Evaluation of the pulsed discharge helium ionization detector for the analysis of hydrogen and methane in breath. *J. Chromatogr. A* **2004**, *1027*, 19–23. [CrossRef] [PubMed]

24. Bogozi, T.; Popp, J.; Frosch, T. Fiber-enhanced Raman multi-gas spectroscopy: What is the potential of its application to breath analysis. *Bioanalysis* **2015**, *7*, 281–284. [CrossRef] [PubMed]

25. Hanf, S.; Bogozi, T.; Keiner, R.; Frosch, T.; Popp, J. Fast and Highly Sensitive Fiber-Enahced Raman Spectroscopic Monitoring of Molecular H_2 and CH_4 for Point-of Care Diagnosis of Malabsorption Disorders in Exhaled Human Breath. *Anal. Chem.* **2015**, *77*, 982–988. [CrossRef] [PubMed]

26. Kien, N.; Hung, C.M.; Ngoc, T.M.; Le, D.T.T.; Hoa, N.D.; Duy, N.V.; Hieu, N.V. Low-temperature prototype hydrogen sensors using Pd-decorated SnO_2 nanowires for exhaled breath applications. *Sens. Actuators B Chem.* **2017**, *253*, 156–163.

27. Gu, H.; Wang, Z.; Hu, Y. Hydrogen Gas Sensors Based on Semiconductor Oxide Nanostructures. *Sensors* **2012**, *12*, 5517–5550. [CrossRef]

28. Hübert, T.; Boon-Brett, L.; Black, G.; Banach, U. Hydrogen sensors—A review. *Sens. Actuators B Chem.* **2011**, *157*, 329–352. [CrossRef]

29. Kim, J.-H.; Mirzaei, A.; Kim, H.W.; Kim, S.S. Improving the hydrogen sensing properties of SnO_2 nanowire-based conductometric sensors by Pd-decoration. *Sens. Actuators B Chem.* **2019**, *285*, 358–367. [CrossRef]

30. Ling, C.; Xue, Q.; Han, Z.; Lu, H.; Xia, F.; Yan, Z.; Deng, L. Room temperature hydrogen sensor with ultrahigh-responsive characteristics based on Pd/SnO2/SiO2/Si heterojunctions. *Sens. Actuators B Chem.* **2016**, *227*, 438–447. [CrossRef]

31. Shim, Y.-S.; Jang, B.; Suh, J.M.; Noh, M.S.; Kim, S.; Han, S.D.; Song, Y.G.; Kang, C.-Y.; Jang, H.W.; Lee, W. Nanogap-controlled Pd coating for hydrogen sensitive switches and hydrogen sensors. *Sens. Actuators B Chem.* **2018**, *255*, 1841–1848. [CrossRef]

32. Korotcenkov, G.; Han, S.D.; Stetter, J.R. Review of electrochemical hydrogen sensors. *Chem. Rev.* **2009**, *109*, 1402–1433. [CrossRef] [PubMed]

33. Wang, M.; Vandermaar, A.J.; Srivastava, K.D. Review of condition assessment of power transformers in service. *IEEE Electr. Insul. Mag.* **2002**, *18*, 12–25. [CrossRef]

34. Perman, J.A.; Modler, S.; Barr, R.G.; Rosenthal, P. Fasting breath hydrogen concentration: Normal values and clinical application. *Gastroenterology* **1984**, *87*, 1358–1363. [CrossRef]

35. Däbritz, J.; Mühlbauer, M.; Domagk, D.; Voos, N.; Henneböhl, G.; Siemer, M.L.; Foell, D. Significance of hydrogen breath tests in children with suspected carbohydrate malabsorption. *BMC Pediatr.* **2014**, *14*, 59. [CrossRef]

36. Park, Y.; Yoo, R.; Park, S.; Lee, J.H.; Jung, H.; Lee, H.-S.; Lee, W. Highly sensitive and selective isoprene sensing performance of ZnO quantum dots for a breath analyzer. *Sens. Actuators B Chem.* **2019**, *290*, 258–266. [CrossRef]

37. McNair, H.M.; Miller, J.M. *Basic Gas Chromatography*, 2nd ed.; John Wiley & Sons Inc.: Hoboken, NJ, USA, 1997.

38. Jung, H.; Cho, W.; Yoo, R.; Lee, H.; Choe, Y.; Jeon, J.Y.; Lee, W. Highly Selective Real-time Detection of Breath Acetone by Using ZnO Quantum Dots with a Miniaturized Gas Chromatographic Column. *Sens. Actuators B Chem.* **2018**, *274*, 527–532. [CrossRef]

39. Batzill, M.; Diebold, U. The surface and materials science of tin oxide. *Prog. Surf. Sci.* **2005**, *79*, 47–154. [CrossRef]

40. Chang, S.C. Oxygen chemisorption on tin oxide: Correlation between electrical conductivity and EPR measurements. *J. Vac. Sci. Technol.* **1980**, *17*, 366–369. [CrossRef]

41. Barsan, N.; Schweizer-Berberich, M.; Gopel, W. Fundamental and practical aspects in the design of nanoscaled SnO_2 gas sensors: A status report. *Fresenius J. Anal. Chem.* **1999**, *365*, 287–304. [CrossRef]

42. Morrison, S.R. Selectivity in semiconductor gas sensors. *Sens. Actuators B* **1987**, *12*, 425–440. [CrossRef]

43. Shivaraman, M.S.; Svensson, C.; Hammarsten, H.; Lundstrom, I. Hydrogen Sensitivity of Palladium-Thin-Oxide-Silicon Schottky Barriers. *Electron. Lett.* **1976**, *12*, 483–484. [CrossRef]

44. Noh, J.; Lee, J.M.; Lee, W. Low-Dimensional Palladium Nanostructures for Fast and Reliable Hydrogen Gas Detection. *Sensors* **2011**, *11*, 825–851. [CrossRef] [PubMed]

45. Cloarec, D.; Bornet, F.; Gouilloud, S.; Barry, J.L.; Salim, B.; Galmiche, J.P. Breath hydrogen response to lactulose in healthy subjects: Relationship to methane producing status. *Gut* **1990**, *31*, 300–304. [CrossRef] [PubMed]

46. Rumessen, J.J.; Hamberg, O.; Gudmand-Høyer, E. Influence of orocaecal transit time on hydrogen excretion after carbohydrate malabsorption. *Gut* **1989**, *30*, 811–814. [CrossRef]

47. Shin, W. Medical applications of breath hydrogen measurements. *Anal. Bioanal. Chem.* **2014**, *406*, 3931–3939. [CrossRef]